

Tailoring the Thermal Conductivity of Two-Dimensional Metal Halide Perovskites

Sandip Thakur,[†] Zhenghong Dai,[‡] Pravin Karna,[†] Nitin P. Padture,[‡] and
Ashutosh Giri^{*,†}

[†]*Department of Mechanical, Industrial and Systems Engineering, University of Rhode Island,
Kingston, RI 02881, USA*

[‡]*School of Engineering, Brown University, Providence, Rhode Island 02912, USA*

E-mail: ashgiri@uri.edu

Sample Preparation and Characterization

Materials

Phenethylammonium iodide (PEAI; 98%, Sigma-Aldrich, USA), lead (II) iodide (PbI_2 ; >98%, TCI), N,N-dimethylformamide (DMF; 99.8%, ACROS Organics, USA), dimethyl sulfoxide (DMSO; 99.7%, ACROS Organics, USA), diethyl ether (DE; >99%, Sigma-Aldrich, USA), hydroiodic acid (HI; 57 wt% in H_2O , Sigma-Aldrich, USA), 4-(aminomethyl)piperdine (4AMP; Sigma-Aldrich, USA), 2-propanol (IPA, Sigma-Aldrich, USA).

Preparation of 4AMPI_2 Powder

At room temperature, 7.5 g of HI was added to the 20 mL of IPA. While stirring, 2.0 g of 4AMP was added to the solution. The solution was stirred overnight, which was followed by the removal of the solvent by using a rotary evaporator. The resulting 4AMPI_2 powder was obtained and stored in a N_2 -filled glovebox.

Deposition of 2D MHP Thin Films

The aluminum transducer deposited glass substrate was treated with UV-ozone treatment for 20 minutes for better wettability prior to the deposition of perovskite thin films. The RP phase precursor solution ($n=1$) was prepared by dissolving 597.6 mg of PEA I and 553.2 mg of PbI_2 in 1 ml of mixed solvent of DMF/DMSO (V/V 4/1). The DJ phase precursor solution ($n=1$) was prepared by dissolving 441.6 mg of 4AMPI_2 and 553.2 mg of PbI_2 in 1 ml of mixed solvent of DMF/DMSO (V/V 4/1). The 2D metal halide perovskite (MHP) thin films were deposited by spin-coating the precursor solution at 5,000 rpm for 20 s. At the 10th second of spinning, 1 mL of anti-solvent DE was dripped onto the center of the spinning substrate. Then, the as-deposited films were annealed at 100 °C for 5 minutes.

Characterization

X-ray diffraction (XRD) was performed to examine the crystalline textures of the MHP films using a high-resolution diffractometer (Discovery D8, Bruker, Germany) in an angle range of $2\theta = 5^\circ$ to 30° . Figure S1 shows the XRD profiles of RP and DJ phase MHP films. The periodic diffraction

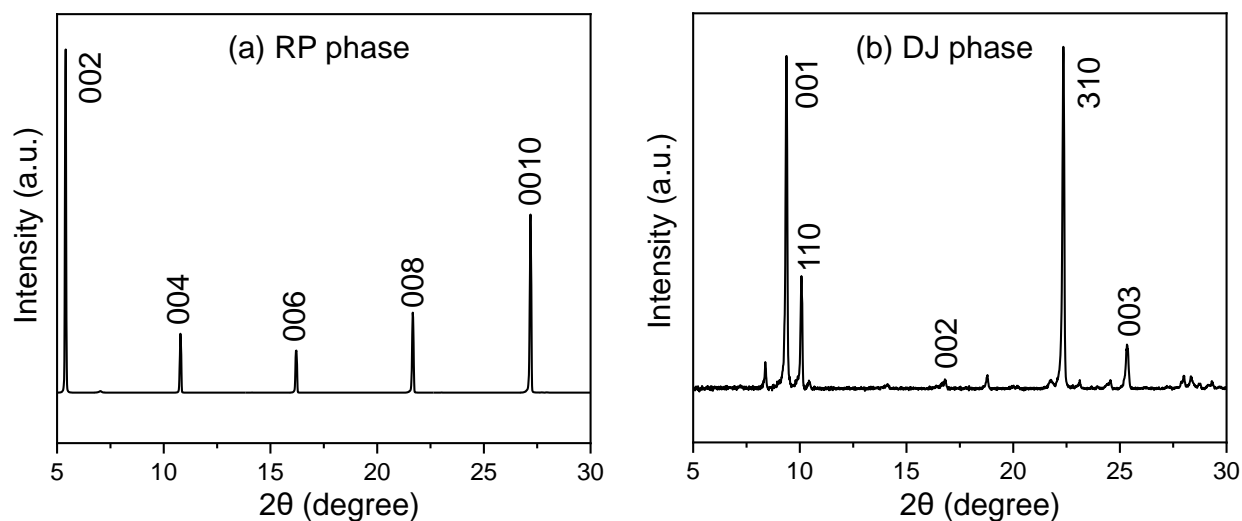


Figure (S1) X-ray diffraction patterns for (a) RP phase $(\text{PEA})_2\text{PbI}_4$ MHP film (b) DJ phase $(4\text{AMP})\text{PbI}_4$ MHP film.

peaks for RP phase as shown in Fig. S1a at 5.5° , 11° , 16.6° , 22° , and 27.5° are assigned to the (002), (004), (006), (008), and (0010) crystal planes, respectively. Similarly, the diffraction peaks for the DJ phase MHP film at 9° , 10° , 16.8° , 22.3° , and 25.3° shown in Fig. S1b are assigned to (001), (110), (002), (310), and (003) crystal planes, respectively. This highlights the excellent crystallinity and shows that the layered structure are preferentially stacked parallel to the substrate.^{1,2} Both the RP and DJ phase MHP films are polycrystalline with grain boundaries. Moreover, the strong low-angle reflections associated with the 2D MHP ($n=1$) indicates preferred in-plane growth (texture) of both RP and DJ phase films. However, in the DJ phase perovskite film, along with mostly parallel growth, there is some vertical growth as well (less texture). We note that this minimal vertical growth should not influence our thermal conductivity measurements for the DJ phase since the anisotropy in thermal conductivity in similar 2D MHPs have been shown to be negligible.³ Also, the unindexed XRD peaks in the DJ phase could be due to some slight degradation byproducts

or minor impurities. This could also affect our thermal conductivity measurements. However, we conjecture that the thermal conductivities in these films are dominated by the polycrystallinity as evidenced by the similar thermal conductivity values for both DJ-based film and RP-based film (without the phase impurities).

Time Domain Thermoreflectance Measurements and Analysis

Time domain thermoreflectance (TDTR) was used to measure the thermal properties of the 2D MHPs. TDTR is a pump-probe technique, in which ~ 100 fs pulses emanate from a Mai Tai Spectra Physics laser at a repetition rate of 80 MHz (~ 12.5 ns time intervals). The pump modulation frequency was set at 10 MHz to create a periodic heating event on the sample surface. Pump and probe beams were focused on nominally ~ 100 nm thick Aluminum (Al) transducer at $1/e^2$ radii values of $11 \mu\text{m}$ and $6 \mu\text{m}$, respectively. The pump and probe beams go through the transparent glass substrate as shown in Fig. 1 of the main manuscript. We monitored the ratio of in-phase to out-of-phase signal voltage ($-V_{\text{in}}/V_{\text{out}}$) of the reflected probe beam using a lock-in amplifier as a function of delay time and fit the data with a thermal model, which accounts for both a three-layer model (i.e. glass substrate/Al/perovskite films) and a two-layer model (glass substrate/Al) for our control sample. The thickness of the Al transducer was accurately measured via picosecond acoustics^{4,5} and was used as an input parameter in the thermal model.

The pump and probe powers were set to 17 mW and 7 mW, respectively. This induces an average surface temperature rise of ~ 15 K as presented in Fig. S2a showing the steady-state surface temperature profile due to laser heating. This temperature rise was accounted for in our thermal model by scaling the heat capacities and thermal conductivities (given as input parameters) accordingly.

Moreover, we note that our pump and probe beams do not directly excite the energy carriers in our 2D MHP films, which could lead to degradation of the films.⁶⁻⁸ This is so because the pump and probe are incident on the 100 nm thick aluminum transducer layer, for which the optical

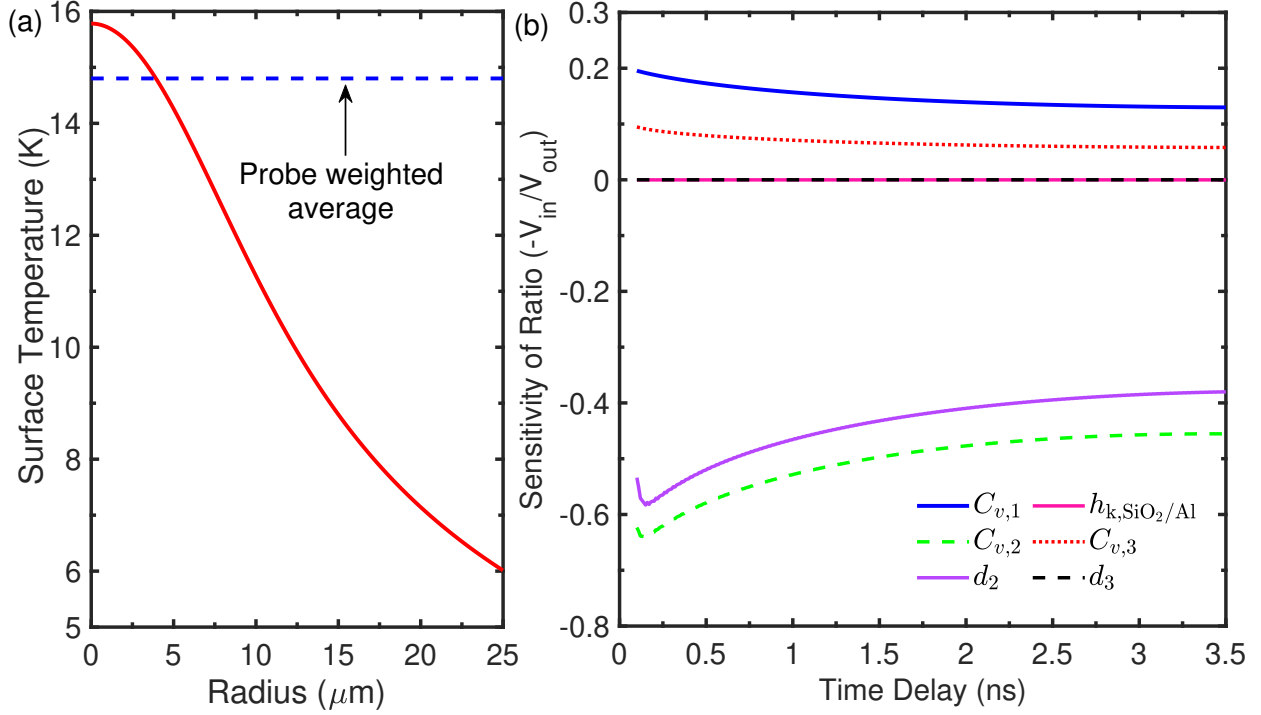


Figure (S2) (a) Increase in surface temperature due to pump pulse heating as a function of radius. The probe weighted average temperature is also included which shows the steady state temperature profile due to pump beam to be 15K. (b) Sensitivities of the ratio of the in-phase and out-of-phase signals to the parameters used in the thermal model. The sensitive parameters in the thermal model are the volumetric heat capacities of the glass substrate ($C_{v,1}$), Al transducer ($C_{v,2}$), and our 2D perovskite films ($C_{v,3}$). The values of ($C_{v,1}$) and ($C_{v,2}$) are taken from prior literature whereas the value of ($C_{v,3}$) is determined via molecular dynamics simulations. Also, we accurately measure the thickness of the Al transducer (d_2) via picosecond acoustics. The other parameters (thermal boundary conductances, h_k across glass/Al interface, and thickness of perovskite films, d_3) have negligible sensitivities to our model.

penetration depth is ~ 11 nm. The optical penetration depth is given as,⁹

$$W = \frac{\lambda}{4\pi k}, \quad (1)$$

where λ is the wavelength of light and k is the damping constant. The characteristic optical penetration depth for Al is calculated to be ~ 10.6 nm, and ~ 5.3 nm for wavelengths (λ) of 800 nm and 400 nm, respectively.

To gauge the accuracy of our TDTR measurements, we define the sensitivity of the ratio to the various thermal properties used in our three-layered thermal model (SiO₂/Al/perovskite films)

by,¹⁰

$$S_x = \frac{\partial \ln(-V_{\text{in}}/V_{\text{out}})}{\partial \ln(x)}, \quad (2)$$

where x is the thermophysical parameter of interest and V_{in} and V_{out} are the in-phase and out-of-phase signals, respectively.

The sensitivities of the ratio to the parameters of interest for ~ 600 nm thick 2D MHP film at 10 MHz pump modulation frequency is shown in Fig. S2b. The volumetric heat capacities of the glass substrate ($C_{v,1}$), Al transducer ($C_{v,2}$), and the 2D MHP films ($C_{v,3}$) are the sensitive parameters in the thermal model. The other parameters (thermal boundary conductances, h_k across glass/Al interface, and thickness of perovskite films, d_3) have negligible sensitivities to our model. The values of the volumetric heat capacities of the aluminum transducer and the glass substrate are taken from prior literature.¹¹

As the heat capacities of the 2D MHPs are unknown in prior literature, we calculated the volumetric heat capacities of the DJ phase and RP phase MHPs via molecular dynamics (MD) simulations as shown in Fig. S3 and is in reasonably good agreement with Ref. [12]. The volumetric heat capacities of our 2D MHPs were determined from the vibrational density of states $D(\omega)$ and applying the Bose-Einstein distribution as,

$$C_v = \int \left(\frac{\hbar\omega}{T} \right)^2 \frac{D(\omega)}{k_B} \frac{e^{\frac{\hbar\omega}{k_B T}}}{(e^{\frac{\hbar\omega}{k_B T}} - 1)^2} d\omega, \quad (3)$$

where κ_B is the Boltzmann constant, T is the temperature, and ω is the angular frequency.

Moreover, as the thickness of the Al transducer (d_2) is also sensitive parameter in the thermal model, we measured its thickness via picosecond acoustics.^{4,5}

Details of the Analysis Procedure

In TDTR experiments, the desired thermal properties were calculated by changing the unknown parameters in a thermal model and fitting them with the experimental TDTR data. Cahill *et al.*,¹³ derived the change in temperature $\theta(r)$ on a metal surface due to laser heating, assuming radial

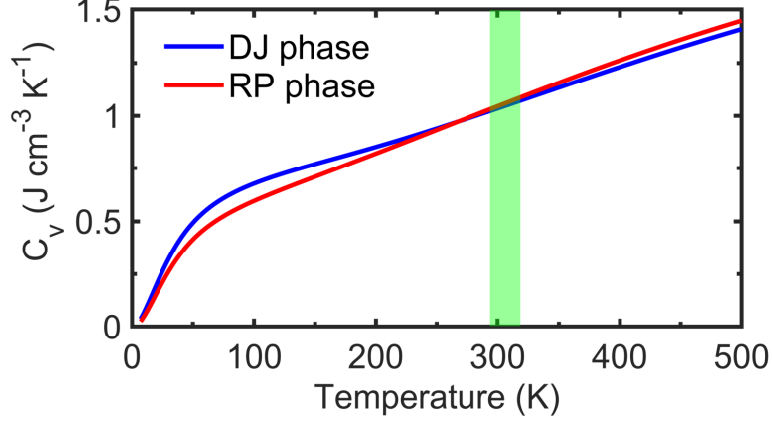


Figure (S3) Volumetric heat capacities of DJ phase and RP phase 2D MHPs as a function of temperature calculated from the vibrational density of states obtained via molecular dynamics simulations.

distribution of heat in a half-sphere from the axially symmetric heat equation in cylindrical coordinates given by,

$$C \frac{\partial \theta(r, z, t)}{\partial t} = \lambda_z \frac{\partial^2 \theta(r, z, t)}{\partial z^2} + \frac{\lambda_r}{r} \frac{\partial}{\partial r} \left(r \frac{\partial \theta(r, z, t)}{\partial r} \right), \quad (4)$$

where λ is the thermal conductivity, r and z represents the radial and through-plane conductivities, and C is the volumetric heat capacity. We apply the Fourier transform (over time) and Hankel transform (over r and z) of Eq. (4), given as,

$$\frac{\partial^2 \theta(r, z, \omega)}{\partial z^2} = q_n^2 \theta(r, z, \omega), \quad (5)$$

$$q_n^2 = \frac{\lambda_r k^2 + iC\omega}{\lambda_z}, \quad (6)$$

where ω is the angular frequency, k is the Hankel transform variable.

For through-plane properties, Eq. (6) is reduced to $q = \sqrt{k^2 + (iC\omega)/\lambda_z}$

The general solution of Eq. (5) is given by,

$$\theta = \underbrace{C_n^1 \exp(q_n z)}_{B^+} + \underbrace{C_n^2 \exp(-q_n z)}_{B^-}, \quad (7)$$

Eq. (7) can be written in matrix form as,

$$\begin{bmatrix} B^+ \\ B^- \end{bmatrix} = \begin{bmatrix} C_n^1 \exp(q_n z) \\ C_n^2 \exp(-q_n z) \end{bmatrix}, \quad (8)$$

The temperature and heat flux in the top layer are related to the bottom layer through,

$$\begin{bmatrix} B_t^+ \\ B_t^- \end{bmatrix} = \begin{bmatrix} \exp(-q_n h) & 0 \\ 0 & \exp(q_n h) \end{bmatrix} \begin{bmatrix} B_b^+ \\ B_b^- \end{bmatrix}, \quad (9)$$

where h is the thickness of materials. For interfacial heat flow, the relation between the temperature at the top layer and bottom layer of the material is given by,

$$\begin{bmatrix} B_n^+ \\ B_n^- \end{bmatrix} = \frac{1}{2\gamma_n} \begin{bmatrix} \exp(-q_n h) & 0 \\ 0 & \exp(q_n h) \end{bmatrix} \begin{bmatrix} \gamma_n + \gamma_{n+1} & \gamma_n - \gamma_{n+1} \\ \gamma_n - \gamma_{n+1} & \gamma_n + \gamma_{n+1} \end{bmatrix} \begin{bmatrix} B_{n+1}^+ \\ B_{n-1}^- \end{bmatrix}, \quad (10)$$

In order to prevent blowing up the temperature, the value of B_n^- in the final layer must be zero.

The thermal response of the system is given by the transfer function $G(k)$ as,

$$G(k) = \frac{1}{\gamma_1} \left(\frac{B_{T1}^+ B_{T1}^-}{B_{T1}^- - B_{T1}^+} \right), \quad (11)$$

where, $\gamma = \lambda_z q_n$, B_{T1}^+ and B_{T1}^- are temperature change coefficients of the material 1.

Further, in order to measure the oscillations of surface temperature of material 1 by cooling from the layers beneath it, we convolute Eq. (11) with the gaussian distribution of pump beam, as

$$\theta(k) = G(k) \frac{A}{2\pi} \exp \left[\frac{-k^2 \omega_0^2}{8} \right], \quad (12)$$

Then we take the weighted average by the radius of the probe beam (ω_1), which gives

$$\theta(r, 0, \omega) = \frac{A}{2\pi} \int_0^\infty G(k) \exp \left[\frac{-k^2 (\omega_0^2 + \omega_1^2)}{8} \right] k dk, \quad (13)$$

where ω_0 and ω_1 are the $1/e^2$ pump and probe beam radius, respectively. Finally, the probe thermorefectance signal is measured via a lock-in amplifier whose output relates the frequency domain signal to the time domain signal given by,

$$\text{Re} \exp[i(\omega_m t + \phi)] = Z(\omega_m) \exp[i\omega_m t], \quad (14)$$

$$Z(\omega_m) = \frac{(2\pi)^2 \chi}{\omega_s^2} \sum_{M=-\infty}^{\infty} \theta(\omega_m + M\omega_s) \exp[iM\omega_s \tau], \quad (15)$$

where ω_m is the pump modulation frequency, $Z(\omega_m)$ is the lock-in transfer function, τ is the pump probe delay time, ω_s is the modulation frequency of the Mai Tai Spectra Physics oscillator, and χ is a constant which is associated with the gain of the electronics.

Molecular Dynamics (MD) Simulations

For our atomistic simulations, we implemented the recently developed MYP potential¹⁴ which can capture a wide array of material properties (such as, structural and dynamical vibrations,¹⁵ elastic properties, ionic polarization^{16,17} and mobility¹⁸). The potential takes into account the nonbonded pairwise interactions by the sum of Lennard-Jones (LJ)/Buckingham and Coulombic terms, which are given as,

$$U = \sum_{i,j} \left[A_{ij} e^{-r_{ij}/\rho_{ij}} - \frac{C_{ij}}{r_{ij}^6} \right] + \sum_{i \neq j} \frac{1}{4\pi\epsilon_0} \frac{q_i q_j}{r_{ij}}, \quad (16)$$

$$U = \sum_{i,j} 4\epsilon_{ij} \left[\left(\frac{\sigma_{ij}}{r_{ij}} \right)^{12} - \left(\frac{\sigma_{ij}}{r_{ij}} \right)^6 \right] + \sum_{i \neq j} \frac{1}{4\pi\epsilon_0} \frac{q_i q_j}{r_{ij}}, \quad (17)$$

Equation (16) takes into account the pairwise interaction between Pb and I atoms along with (Pb, I)-(C, N) whereas, Equation (17) defines all other remaining pairwise interactions.

Class II Force Field

We used the class2 potential to define our bonded interactions between the organic cations. Class II force field is a general all-atom force field which incorporates van der Waals forces, bond angles, dihedrals, and improper interactions. This class II force field has been used extensively for modeling inorganic and organic structures.^{19,20} The full functional form of the potential is given as,

$$\begin{aligned}
 E_{total} = & \sum_b [K_2(b - b_0)^2 + K_3(b - b_0)^3 + K_4(b - b_0)^4] \\
 & + \sum_\theta [D_2(\theta - \theta_0)^2 + D_3(\theta - \theta_0)^3 + D_4(\theta - \theta_0)^4] \\
 & + \sum_\phi [V_1(1 - \cos(\phi - \phi_1)) + V_2(1 - \cos(2\phi - \phi_2)) + V_3(1 - \cos(3\phi - \phi_3))] \\
 & + \sum_\chi K_2\chi^2 + \sum_{b,b'} F_{bb'}(b - b_0)(b' - b'_0) + \sum_{b,\theta} F_{b\theta}(b - b_0)(\theta - \theta_0) \\
 & + \sum_{b,\phi} F_{b\phi}(b - b_0)[H_1 \cos \phi + H_2 \cos 2\phi + H_3 \cos 3\phi] \\
 & + \sum_{\theta,\phi} (\theta - \theta_0)[H_1 \cos \phi + H_2 \cos 2\phi + H_3 \cos 3\phi] \\
 & + \sum_{\theta,\theta'} F_{\theta,\theta'}(\theta' - \theta'_0)(\theta - \theta_0) + \sum_{\phi,\theta,\theta'} F_{\phi,\theta,\theta'} \cos \phi(\theta - \theta_0)(\theta' - \theta'_0) \\
 & + \sum_{i>j} \frac{q_i q_j}{r_{ij}} + \sum_{ij} \epsilon_{ij} \left[2\left(\frac{\sigma_{ij}}{r_{ij}}\right)^2 - 3\left(\frac{\sigma_{ij}}{r_{ij}}\right)^6 \right]
 \end{aligned} \tag{18}$$

Table (S1) Parameters used to model CH_3NH_3^+ under the class II force field.

Bond Coefficients				
Type	b_0	K_2	K_3	K_4
1	1.0260	483.4512	0.0000	0.0000
2	1.4200	280.0000	0.0000	0.0000
3	1.4170	470.8361	-627.6179	1327.6345
4	1.0982	372.8251	-803.4526	894.3173
5	1.0100	462.7500	-1053.6300	1545.7570

Angle Coefficients

Type	θ_0	D_2	D_3	D_4
1, 2, 9	122.0000	35.0000	0.0000	0.0000
3	118.9000	61.0226	-34.9931	0.0000
4	120.0000	37.0000	0.0000	0.0000
5	120.0000	102.0000	0.0000	0.0000
6	120.0000	37.0000	0.0000	0.0000
7	117.9400	35.1558	-12.4682	0.0000
8	116.9402	37.5749	-8.6676	0.0000

Dihedral Coefficients

Type	V_1	ϕ_1	V_2	ϕ_2	V_3	ϕ_3
1, 2, 8, 9	0.0000	0.0000	2.2500	0.0000	0.0000	0.0000
3	0.0000	0.0000	3.9661	0.0000	0.0000	0.0000
4	8.3667	0.0000	1.1932	0.0000	0.0000	0.0000
5, 6	0.0000	0.0000	3.0000	0.0000	0.0000	0.0000
7	0.0000	0.0000	1.8769	0.0000	0.0000	0.0000

Bond-Bond Coefficients

Type	$F_{bb'}$	b_0	b'_0
1	0.0000	1.0260	1.0260
2	0.0000	1.0260	1.4200
3	68.2856	1.4170	1.4170
4	0.0000	1.4200	1.0982
5	0.0000	1.4200	1.4170
6	0.0000	1.0982	1.0982
7	1.0795	1.0982	1.4170
8	-0.5655	1.0100	1.0100
9	0.0000	1.0100	1.4200

Bond-Angle Coefficients

Type	$F_{b\theta,1}$	$F_{b\theta,2}$	b_{01}	b_{02}
1	0.0000	0.0000	1.0260	1.0260
2	0.0000	0.0000	1.0260	1.4200
3	28.8708	28.8708	1.4170	1.4170
4	0.0000	0.0000	1.4200	1.0982
5	0.0000	0.0000	1.4200	1.4170
6	0.0000	0.0000	1.0982	1.0982
7	24.2183	20.0033	1.0982	1.4170
8	19.8125	19.8125	1.0100	1.0100
9	0.0000	0.0000	1.0100	1.4200

Angle-Angle Torsion Coefficients

Type	$F_{\theta,\theta'}$	θ_0	θ'_0
1, 2, 8, 9	0.0000	122.0000	120.0000
3	-4.8141	118.9000	117.9400
4	0.0000	118.9000	118.9000
5	0.0000	120.0000	118.9000
6	0.0000	120.0000	117.9400
7	0.3598	117.9400	117.9400

Middle-Bond Torsion Coefficients

Type	H_1	H_2	H_3	b_0
1, 2, 8, 9	0.0000	0.0000	0.0000	1.4200
3	0.0000	-1.1521	0.0000	1.4170
4	27.5989	-2.3120	0.0000	1.4170
5, 6	0.0000	0.0000	0.0000	1.4170
7	0.0000	4.8228	0.0000	1.4170

Non-equilibrium MD (NEMD) Simulation

The thermal conductivity of our DJ phase and RP phase perovskites are evaluated by NEMD method using the LAMMPS package.²¹ In this method, we impose a heat flux across the computational domain in a particular direction by prescribing a ‘hot’ region located at one end of the simulation box and extracting the equal amount of heat from the ‘cold’ region located at the other end of the simulation box. This induces a temperature gradient across the simulation box.

After we obtained a steady-state temperature profile, the thermal conductivity was calculated by invoking the Fourier’s law of heat conduction,

$$\dot{Q} = -\kappa \frac{dT}{dx}, \quad (19)$$

where \dot{Q} is the rate of heat flux added and subtracted from the hot and cold regions, κ is the thermal conductivity, and $\frac{dT}{dx}$ is the temperature gradient averaged over time and space.

Considering the effect of simulation box size (i.e. strong scattering of long wavelength phonons near and at the heat source/sink region),²²⁻²⁴ we extrapolated the thermal conductivity value to the

limit of an infinite system length (i.e. $\kappa_{L \rightarrow \infty}$). The relation between the inverse thermal conductivity and inverse system length is given by following equation when the length of the system is comparable or larger than the phonon average mean free path (λ):

$$\frac{1}{\kappa(L)} = \frac{1}{\kappa_{L \rightarrow \infty}} \left(1 + \frac{\lambda}{L} \right), \quad (20)$$

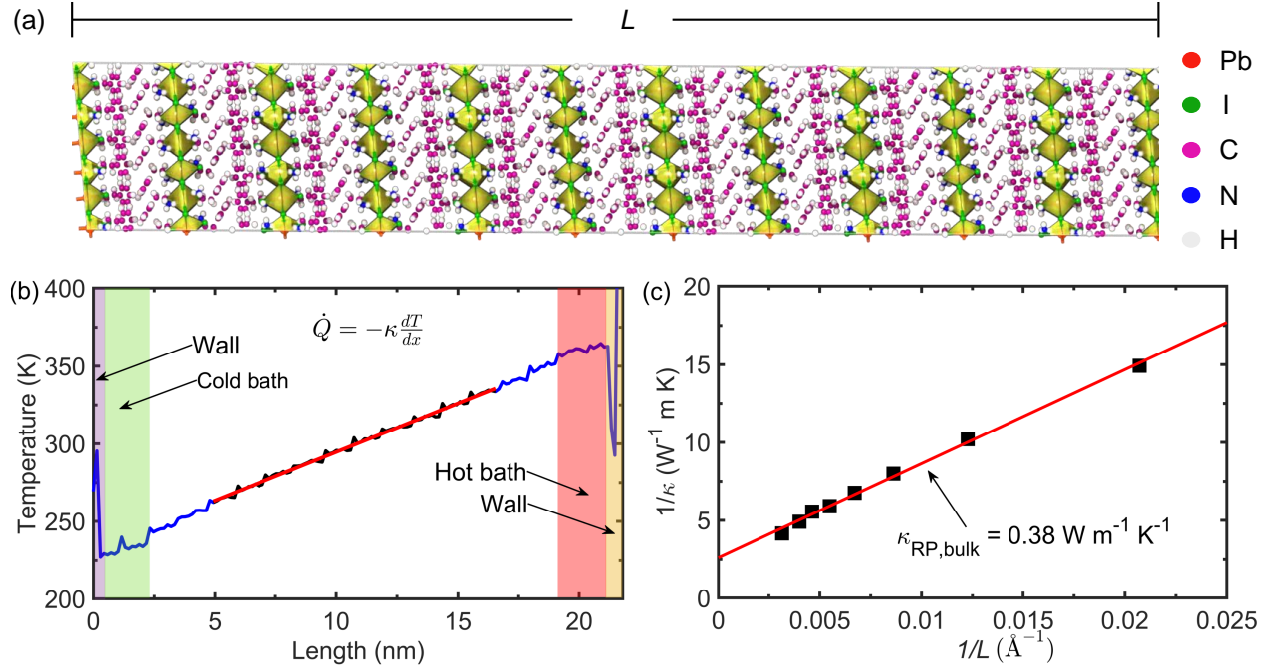


Figure (S4) (a) Schematic illustration of the computational domain for our RP phase MHP structure used in our NEMD simulations to predict the through-plane thermal conductivities. (b) Steady-state temperature profile obtained from our NEMD simulation, which we utilize to calculate the thermal conductivity by invoking the Fourier's law. (c) NEMD-predicted inverse of size-dependent thermal conductivities as a function of the inverse of the computational domain length in the applied heat flux direction. The extrapolation of the linear fits to $1/L \rightarrow 0$ predicts the thermal conductivity of the 'bulk' system.

Figures S4 and S5 show the details of the NEMD simulations carried out on the 2D MHPs (RP phase and DJ phase) in the through-plane direction. We calculated the thermal conductivity for different simulation box length ranging from 100 to 450 Å using a timestep of 1 fs.

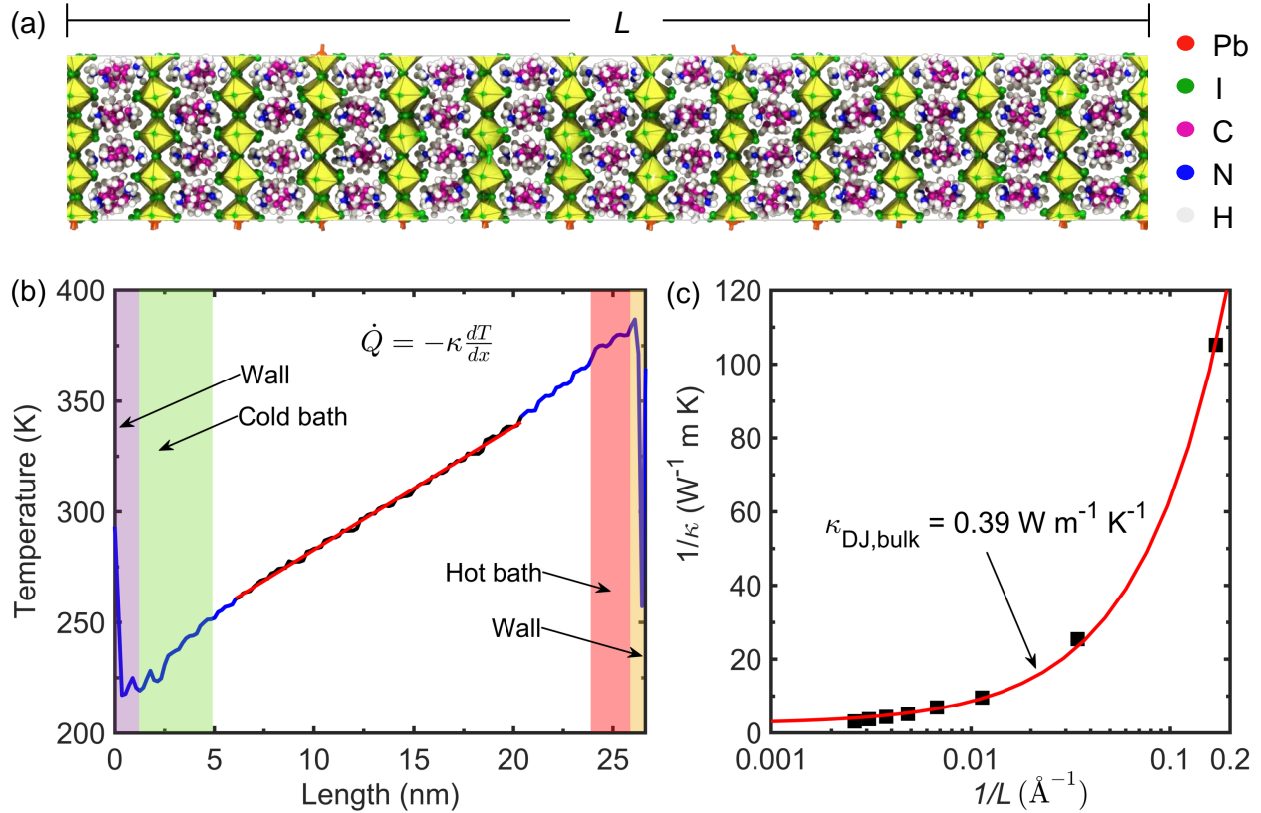


Figure (S5) (a) Schematic illustration of the computational domain for our DJ phase MHP structure used in our NEMD simulations to predict the through-plane thermal conductivities. (b) Steady-state temperature profile obtained from our NEMD simulation, which we utilize to calculate the thermal conductivity by invoking the Fourier's law. (c) NEMD-predicted inverse of size-dependent thermal conductivities as a function of the inverse of the computational domain length in the applied heat flux direction. The extrapolation of the linear fits to $1/L \rightarrow 0$ predicts the thermal conductivity of the 'bulk' system.

Table (S2) Computational domain lengths with corresponding total number of atoms for (a) DJ and (b) RP phase MHPs structure in our NEMD simulations.

(a) DJ phase		(b) RP phase	
Domain length (nm)	Number of atoms (N)	Domain length (nm)	Number of atoms (N)
10	3,960	13.6	6,768
12.5	4,736	17.0	8,460
17.5	6,960	20.4	10,152
23.6	9,280	23.7	11,844
29.5	11,600	27.0	13,536
35.4	13,920	30.4	15,228
41.2	16,240	33.8	16,920
47.0	18,560	40.6	20,304

For our equilibration process, the structures are initially equilibrated under the Nose-Hoover thermostat and barostat (i.e. the NPT ensemble)²⁵ for 1 ns with a timestep of 0.5 fs where the number of particles, pressure and temperature of the system were held constant at 0 bar pressure. Following the NPT integration, further equilibration was carried out under the NVT ensemble where the volume and temperature were kept constant for a total of 1 ns with periodic boundary conditions in all three directions for the entire simulation. An additional equilibration was performed under NVE ensemble for 1 ns where number of particles, volume and total energy of the system were maintained constant. Finally, we utilized the NEMD method to calculate the thermal conductivities of the computational domains, under the microcanonical ensemble (or NVE ensemble). The size of both the cold and hot baths are 40 Å. The local average temperature calculated every 10000 timesteps was obtained by dividing the system length into 150 equally spaced bins in the direction of heat flux applied which is given by,²²

$$\langle T(z) \rangle = \frac{1}{M} \sum_{i=0}^{M-1} T_{N-i}(z), \quad (21)$$

where $\langle T(z) \rangle$ is the average temperature at z over the final M time steps of the simulation, $T_{N-i}(z)$ is the instantaneous temperature at location z for the $N-i$ timestep and N denotes the total number of simulation steps.

Figure S6 shows the details of the additional NEMD simulations performed on 3D MAPbI₃ structure in the through-plane direction. The initial computational domain of the 3D structure was equilibrated under the Nose-Hoover thermostat and barostat using the NPT integration for a total of 1 ns at 0 bar pressure using a timestep of 0.5 fs followed by an NVT integration where the volume and temperature was kept constant for a total of 1 ns with periodic boundary conditions in all three directions for the entire simulation. Further, an additional equilibration was performed under NVE ensemble for 1 ns where number of particles, volume and total energy of the system were maintained constant. Finally, we utilized the NEMD method to calculate the thermal conductivities of the computational domains, under the NVE ensemble.

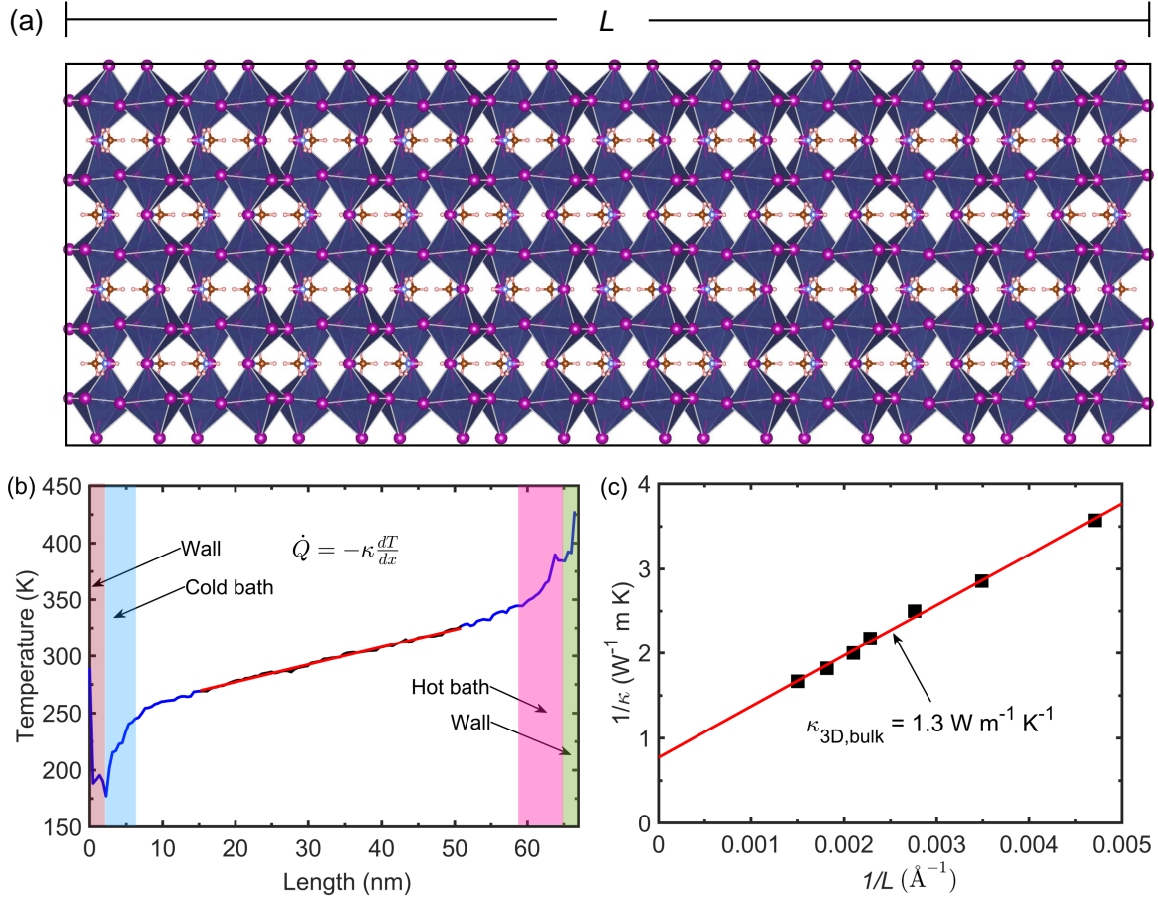


Figure (S6) (a) (a) Schematic illustration of the computational domain for 3D MAPbI₃ MHP structure used in our NEMD simulations to predict the through-plane thermal conductivities. (b) Steady-state temperature profile obtained from our NEMD simulation, which we utilize to calculate the thermal conductivity by invoking the Fourier's law. (c) NEMD-predicted inverse of size-dependent thermal conductivities as a function of the inverse of the computational domain length in the applied heat flux direction. The extrapolation of the linear fits to $1/L \rightarrow 0$ predicts the thermal conductivity of the 'bulk' system.

Vibrational Density of States

For the calculation of vibrational density of states (vDOS) of our 2D perovskite structures, we output the velocities of the atoms every 10 time steps for a total time of 1 ns. After the collection of the velocity fluctuation time series, we performed the fourier transformation of the velocity autocorrelation function (VACF) algorithm. Furthermore, the Welch method of power spectral

(a) DJ phase with longer organic spacer length

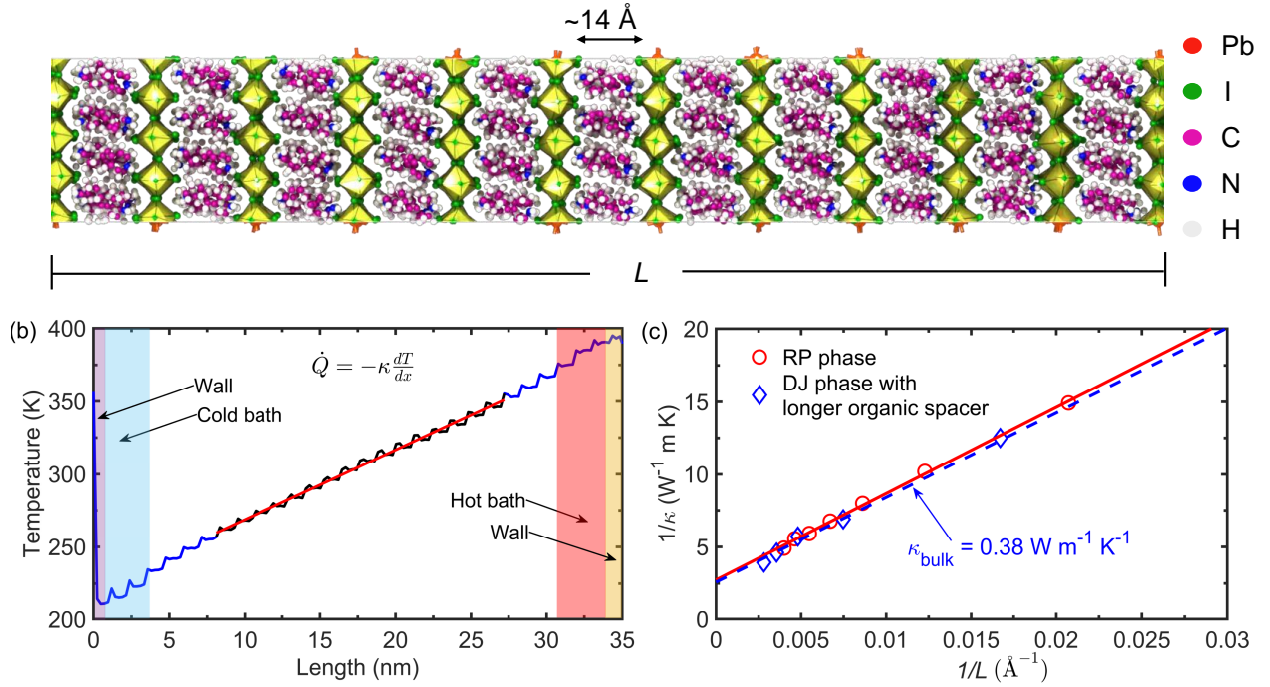


Figure (S7) (a) Schematic illustration of the computational domain for our DJ phase MHP structure with longer organic spacer length ($\sim 14 \text{ \AA}$) used in our NEMD simulations to predict the through-plane thermal conductivities. (b) Steady-state temperature profile obtained from our NEMD simulation, which we utilize to calculate the thermal conductivity by invoking the Fourier's law. (c) NEMD-predicted inverse of size-dependent thermal conductivities for RP and DJ phase with longer organic space length as a function of the inverse of the computational domain length in the applied heat flux direction. The extrapolation of the linear fits to $1/L \rightarrow 0$ predicts the thermal conductivity of the 'bulk' system. Although weaker van der Waals interactions exists in the RP phase perovskite compared to the DJ phase, the similarity in the thermal conductivities for our RP phase and a DJ phase perovskite with a longer organic spacer that matches the spacer length in the RP phase suggests that the van der Waals interactions has negligible influence in dictating the thermal transport properties in these hybrid perovskites.

density estimation was applied to obtain the vDOS as,

$$D(\omega) = \frac{1}{2k_{\text{B}}T} m(\text{VACF})\rho, \quad (22)$$

where, m is the atomic mass. k_{B} , T , and ρ are the Boltzmann constant, local temperature, and atomic density, respectively.

The vibrational density of states for both the DJ and RP MHP phase is shown in Fig. S8. For both the phases, there is negligible difference in the vDOS with comparable spectral bandwidths.

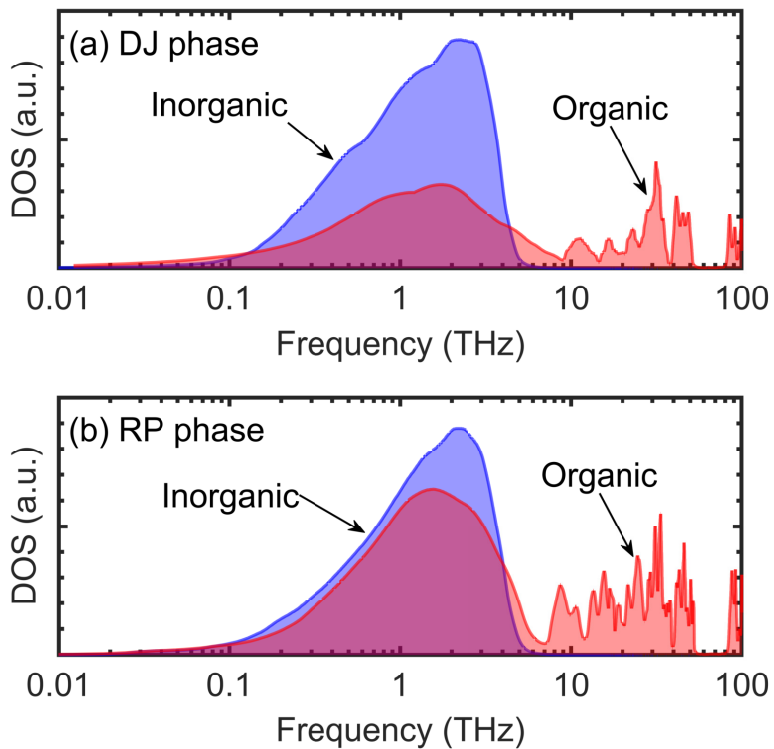


Figure (S8) Vibrational density of states of our relaxed (a) DJ phase MHP structure and (b) RP phase MHP structure.

Both phases encompass a broad spectral range (up to and greater than 50 THz). The higher energy vibrations are solely due to the bond bending, stretching which are the direct consequences of the strong C-H, C-N and N-H bonds.^{12,14}

Green-Kubo (GK) Method

Following the NEMD simulation, the Green-Kubo (GK) formalism was used to qualitatively evaluate the thermal conductivity of our equilibrated molecular structures with decreasing spacing between the organic cations, which is given as,

$$\kappa_{\alpha} = \frac{1}{k_{\text{B}}VT^2} \int_0^{\infty} \langle J_{\alpha}(t)J_{\alpha}(0) \rangle dt, \quad (23)$$

where t is the time, T and V are the temperature and volume of the system, and $\langle J_\alpha(t)J_\alpha(0) \rangle$ is the α th component of the heat current autocorrelation function (HCACF) which is given as,

$$J = \frac{1}{V} \left(\sum_i v_i \epsilon_i + \sum_i S_i \cdot v_i \right), \quad (24)$$

where, v_i , ϵ_i , and S_i represent the velocity, energy and stress of atom i , respectively.

In order to predict the organic and inorganic contribution to the overall thermal conductivity in our 2D MHPs structure, we separated the organic and inorganic groups in our atomistic simulations and output the heat currents for organic and inorganic groups separately every 14 timesteps with a time step of 0.5 fs. Following this we used Eq. (23) to compute the thermal conductivity of each group individually using the GK formalism. The reason we used GK simulations to simulate the qualitative effect of decreasing organic cation spacing is mainly due to the computational cost of the NEMD simulations along with the advantage of separating the contributions to the total heat flux from the organic and inorganic constituents. However, we note that the description of atomic stress as used in the GK formalism in LAMMPS has been shown to produce erroneous results on multi-body potentials.^{26,27} Therefore, we only made a qualitative comparison based on our GK results for the purposes of this work.

Electronic band Gap Calculations

In order to verify that the overall thermal conductivity of our MHPs are solely dictated by lattice vibrations and not by the electronic subsystem, we carried out first-principles calculations using the commercially available software package Quantum Espresso under the density functional theory framework.^{28,29} We perform SCF (self-consistent field) calculations to calculate the electronic band gap of the DJ and RP phases of our MHPs. For these calculations, we utilize the Perdew-Burke-Ernzerhof (PBE) exchange-correlation functional and a plane-wave basis with an energy cut-off of 50 Ry. A uniform k -mesh grid of $4 \times 4 \times 4$ is used for both (4AMP)PbI₄ and (PEA)₂PbI₄. We obtain a band gap of 1.8 eV and 1.9 eV for DJ and RP phases, respectively, which is comparable to the

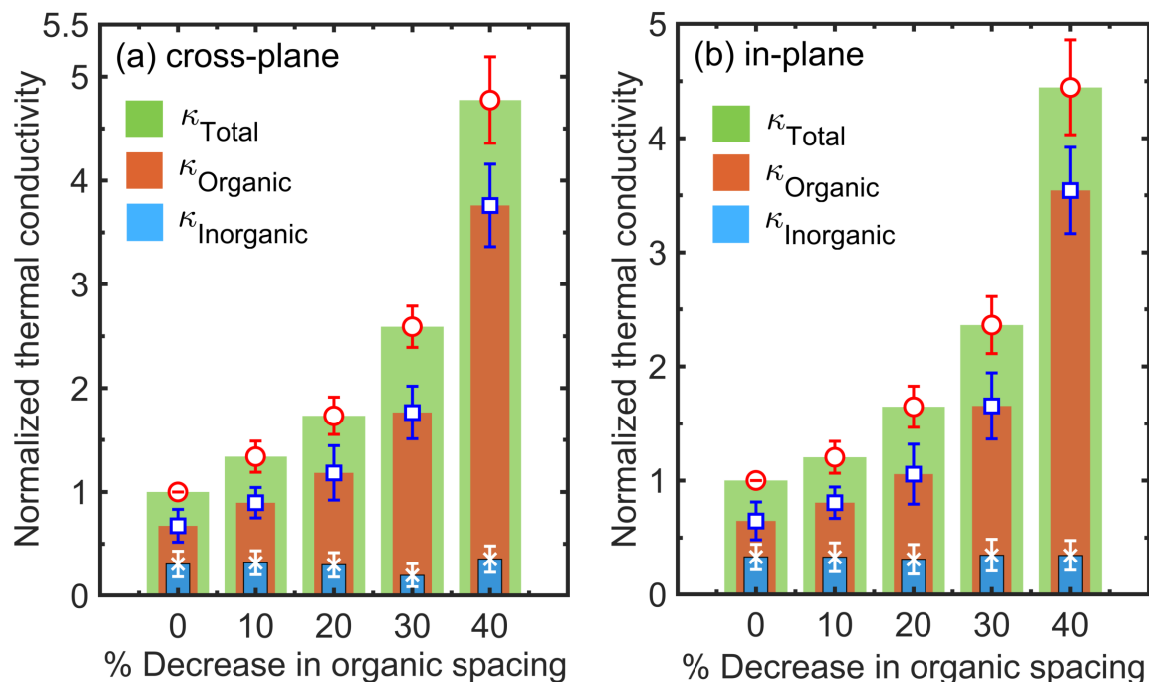


Figure (S9) Normalized thermal conductivities (with respect to the RP phase) in the (a) through-plane (b) in-plane directions as a function of percentage decrease in distance between the organic cations (d) for our RP phase. In both directions, decreasing d leads to enhanced heat transfer mainly driven by the organic cations in both the through-plane and in-plane directions.

band gaps calculated for similar MHPs in prior literatures.^{30,31} The considerable band gaps in both the DJ and RP phase MHPs supports our claim that there is no electronic contribution to the overall thermal conductivity predicted in our study. Moreover, we performed additional DFT simulations to calculate the electronic band gap of the compressed DJ structure with reduced spacing between the adjacent organic cations (at 40% decrease in cation separation lengths). The significant band gap of 2.07 eV calculated for the DJ structure even with reduced organic spacing shows that this structure is semiconducting in nature for the strains applied in this work, and so the thermal transport in these systems are still vibrationally-driven.

Furthermore, we have performed additional DFT calculations to assess the thermodynamic structural stability for our compressed DJ structure with 40% reduction in the organic spacing. We determined the cohesive energies by calculating the difference between the energies of structures compared to the energy of a single atom using the same pseudopotential and calculation parameters. The calculated cohesive energy for our DJ structure with reduced organic spacing is 88.68

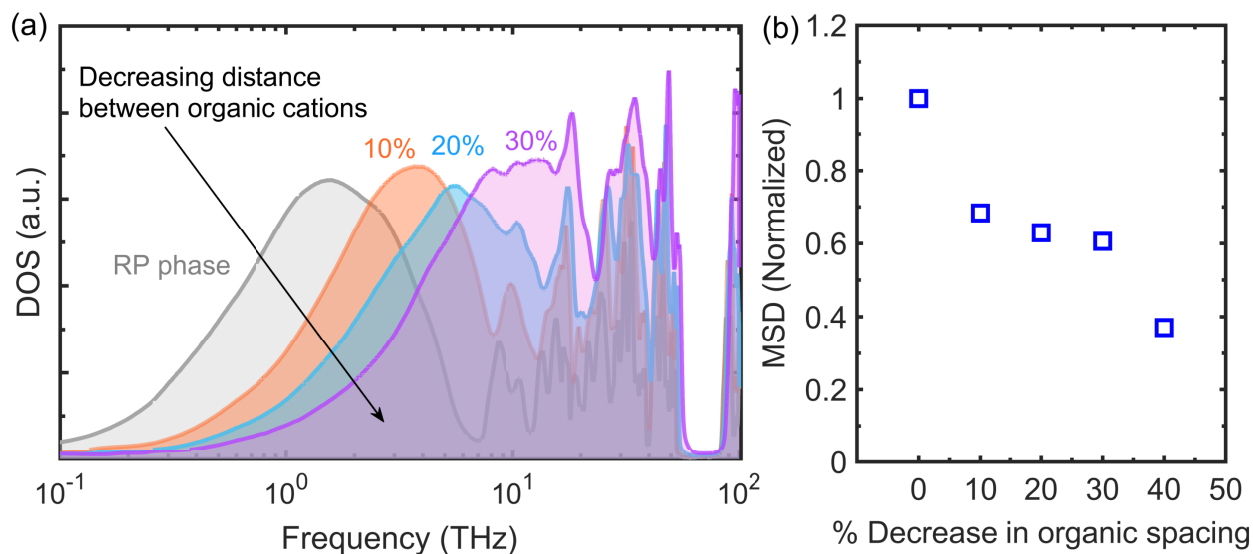


Figure (S10) (a) Vibrational density of states of our RP phase for the decreased spacing between organic cations compared to that of the realistic structure. The low frequency vibrations shifts to the higher frequencies with decreasing spacing between the organic cations attributed to vibrational hardening. (b) Calculated mean square displacements of the organic cations as a function of decreasing distance between the organic cations. The mean square displacements of the atoms decreases due to vibrational hardening which leads to an increase in the overall thermal conductivity.

Ry/atom and the average cohesive energy calculated from the energies of single atom computations is 88.35 Ry/atom. The similarity between the two values indicate that our structures are thermodynamically stable.³²

References

- (1) Li, M.-H.; Yeh, H.-H.; Chiang, Y.-H.; Jeng, U.-S.; Su, C.-J.; Shiu, H.-W.; Hsu, Y.-J.; Kotsugi, N.; Ohigashi, T.; Chen, Y.-A., et al. Highly efficient 2D/3D hybrid perovskite solar cells via low-pressure vapor-assisted solution process. *Advanced Materials* **2018**, *30*, 1801401.
- (2) Hu, R.; Zhang, Y.; Paek, S.; Gao, X.-X.; Li, X.; Nazeeruddin, M. K. Enhanced stability of α -phase FAPbI₃ perovskite solar cells by insertion of 2D (PEA)₂PbI₄ nanosheets. *Journal of materials chemistry A* **2020**, *8*, 8058–8064.
- (3) Li, C.; Ma, H.; Li, T.; Dai, J.; Rasel, M. A. J.; Mattoni, A.; Alatas, A.; Thomas, M. G.; Rouse, Z. W.; Shragai, A.; Baker, S. P.; Ramshaw, B. J.; Feser, J. P.; Mitzi, D. B.; Tian, Z. Remarkably Weak Anisotropy in Thermal Conductivity of Two-Dimensional Hybrid Perovskite Butylammonium Lead Iodide Crystals. *Nano Letters* **2021**, *21*, 3708–3714.
- (4) Tas, G.; Maris, H. J. Electron diffusion in metals studied by picosecond ultrasonics. *Physical Review B* **1994**, *49*, 15046.
- (5) Thomsen, C.; Strait, J.; Vardeny, Z.; Maris, H. J.; Tauc, J.; Hauser, J. Coherent phonon generation and detection by picosecond light pulses. *Physical review letters* **1984**, *53*, 989.
- (6) Fang, H.-H.; Yang, J.; Tao, S.; Adjokatse, S.; Kamminga, M. E.; Ye, J.; Blake, G. R.; Even, J.; Loi, M. A. Unravelling Light-Induced Degradation of Layered Perovskite Crystals and Design of Efficient Encapsulation for Improved Photostability. *Advanced Functional Materials* **2018**, *28*, 1800305.
- (7) Nie, L.; Ke, X.; Sui, M. Microstructural study of two-dimensional organic-inorganic hybrid perovskite nanosheet degradation under illumination. *Nanomaterials* **2019**, *9*, 722.
- (8) Parashar, M.; Kaul, A. B. Methylammonium Lead Tri-Iodide Perovskite Solar Cells with Varying Equimolar Concentrations of Perovskite Precursors. *Applied Sciences* **2021**, *11*, 11689.

- (9) Hummel, R. E. *Electronic properties of materials*; Springer, 2011; Vol. 3.
- (10) Costescu, R. M.; Wall, M. A.; Cahill, D. G. Thermal conductance of epitaxial interfaces. *Physical Review B* **2003**, *67*, 054302.
- (11) Ho, C. Y.; Powell, R. W.; Liley, P. E. Thermal conductivity of the elements. *Journal of Physical and Chemical Reference Data* **1972**, *1*, 279–421.
- (12) Giri, A.; Chen, A. Z.; Mattoni, A.; Aryana, K.; Zhang, D.; Hu, X.; Lee, S.-H.; Choi, J. J.; Hopkins, P. E. Ultralow thermal conductivity of two-dimensional metal halide perovskites. *Nano letters* **2020**, *20*, 3331–3337.
- (13) Cahill, D. G. Analysis of heat flow in layered structures for time-domain thermoreflectance. *Review of scientific instruments* **2004**, *75*, 5119–5122.
- (14) Mattoni, A.; Filippetti, A.; Saba, M.; Delugas, P. Methylammonium rotational dynamics in lead halide perovskite by classical molecular dynamics: the role of temperature. *The Journal of Physical Chemistry C* **2015**, *119*, 17421–17428.
- (15) Mattoni, A.; Filippetti, A.; Saba, M.; Caddeo, C.; Delugas, P. Temperature evolution of methylammonium trihalide vibrations at the atomic scale. *The Journal of Physical Chemistry Letters* **2016**, *7*, 529–535.
- (16) Caddeo, C.; Filippetti, A.; Mattoni, A. The dominant role of surfaces in the hysteretic behavior of hybrid perovskites. *Nano Energy* **2020**, *67*, 104162.
- (17) Mattoni, A.; Caddeo, C. Dielectric function of hybrid perovskites at finite temperature investigated by classical molecular dynamics. *The Journal of Chemical Physics* **2020**, *152*, 104705.
- (18) Delugas, P.; Caddeo, C.; Filippetti, A.; Mattoni, A. Thermally activated point defect diffusion in methylammonium lead trihalide: anisotropic and ultrahigh mobility of iodine. *The journal of physical chemistry letters* **2016**, *7*, 2356–2361.

- (19) Maple, J. R.; Dinur, U.; Hagler, A. T. Derivation of force fields for molecular mechanics and dynamics from ab initio energy surfaces. *Proceedings of the National Academy of Sciences* **1988**, *85*, 5350–5354.
- (20) Sun, H. COMPASS: an ab initio force-field optimized for condensed-phase applications overview with details on alkane and benzene compounds. *The Journal of Physical Chemistry B* **1998**, *102*, 7338–7364.
- (21) Plimpton, S. Fast parallel algorithms for short-range molecular dynamics. *Journal of computational physics* **1995**, *117*, 1–19.
- (22) Schelling, P. K.; Phillpot, S. R.; Keblinski, P. Comparison of atomic-level simulation methods for computing thermal conductivity. *Physical Review B* **2002**, *65*, 144306.
- (23) Tang, Q. A molecular dynamics simulation: the effect of finite size on the thermal conductivity in a single crystal silicon. *Molecular Physics* **2004**, *102*, 1959–1964.
- (24) Jund, P.; Jullien, R. Molecular-dynamics calculation of the thermal conductivity of vitreous silica. *Physical review B* **1999**, *59*, 13707.
- (25) Hoover, W. G. Canonical dynamics: Equilibrium phase-space distributions. *Physical review A* **1985**, *31*, 1695.
- (26) Surblys, D.; Matsubara, H.; Kikugawa, G.; Ohara, T. Application of atomic stress to compute heat flux via molecular dynamics for systems with many-body interactions. *Physical Review E* **2019**, *99*, 051301.
- (27) Boone, P.; Babaei, H.; Wilmer, C. E. Heat flux for many-body interactions: corrections to LAMMPS. *Journal of chemical theory and computation* **2019**, *15*, 5579–5587.
- (28) Giannozzi, P.; Baroni, S.; Bonini, N.; Calandra, M.; Car, R.; Cavazzoni, C.; Ceresoli, D.; Chiarotti, G. L.; Cococcioni, M.; Dabo, I., et al. QUANTUM ESPRESSO: a modular and

- open-source software project for quantum simulations of materials. *Journal of physics: Condensed matter* **2009**, *21*, 395502.
- (29) Giannozzi, P.; Andreussi, O.; Brumme, T.; Bunau, O.; Nardelli, M. B.; Calandra, M.; Car, R.; Cavazzoni, C.; Ceresoli, D.; Cococcioni, M., et al. Advanced capabilities for materials modelling with Quantum ESPRESSO. *Journal of physics: Condensed matter* **2017**, *29*, 465901.
- (30) Yin, J.; Naphade, R.; Maity, P.; Gutiérrez-Arzaluz, L.; Almalawi, D.; Roqan, I. S.; Brédas, J.-L.; Bakr, O. M.; Mohammed, O. F. Manipulation of hot carrier cooling dynamics in two-dimensional Dion–Jacobson hybrid perovskites via Rashba band splitting. *Nature communications* **2021**, *12*, 1–9.
- (31) Mao, L.; Ke, W.; Pedesseau, L.; Wu, Y.; Katan, C.; Even, J.; Wasielewski, M. R.; Stoumpos, C. C.; Kanatzidis, M. G. Hybrid Dion–Jacobson 2D lead iodide perovskites. *Journal of the American Chemical Society* **2018**, *140*, 3775–3783.
- (32) Ji, W.; Zhang, L.; Liew, K. A “fullerene-carbon nanotube” structure with tunable mechanical properties. *EPL (Europhysics Letters)* **2018**, *121*, 56001.